A Non-gradient Model of Turbulent Gas Fluxes over Land Surfaces

Y. Tang[1], S. Shahnaz[1,2], and J. Wang[1]

[1]School of Civil and Environmental Engineering, Georgia Institute of Technology, 790 Atlantic Dr NW, Atlanta, GA 30313, USA.

[2]Department of Civil and Construction Engineering, Kennesaw State University, MD # 9055, 655 Arnston Drive, Marietta, GA 30060, USA.

Corresponding author: Yao Tang (yao.tang72@gmail.com)

Key Points:

- Turbulent gas fluxes calculated from near surface single-level gas concentration data without using concentration gradient, wind speed, or surface roughness data
- Estimation of water vapor and CO_2 fluxes over contrasting climate and vegetation conditions at diurnal and seasonal scales

Abstract

A novel non-gradient model is formulated for estimating gas fluxes using single-level time-series data of near-surface gas concentration over land surfaces. When the vertical turbulent transport process in the atmospheric surface layer is described by a one-dimensional diffusion equation, a gas flux is expressed as a weighted integral of the time-history of single-level gas concentration. The eddy-diffusivity may be parameterized as a function of sensible heat flux based on the Monin-Obukhov similarity theory without explicit dependence on wind speed and surface roughness. Sensible heat flux may be estimated from net radiation and surface temperature using the maximum entropy production model. Case studies at six sites with diverse vegetation covers, geographic and climatic conditions at sub-daily scale demonstrate the model's ability to simulate diurnal variations of water vapor and CO_2 fluxes using fewer inputs than other models. Good performance of the model at seasonal scale suggests that the proposed model is a promising tool for the assessment of annual water and carbon budgets over vegetated land surfaces.

Keywords*:* Surface gas fluxes; single-level gas concentration; non-gradient model.

1. Introduction

Fluxes of greenhouse gases such as water vapor and CO_2 over land surfaces are commonly estimated using the bulk transfer models (BTM) [*Collatz et al.*, 1991; *Lee and Pielke*, 1992; *Philip*, 1957; *Sellers et al.*, 1997; *Sellers et al.*, 1996; *Wang and Dickinson*, 2012]. In the BTMs, the bulk gas flux is expressed as the bulk gradient of gas concentration at two levels separated by a short distance multiplied by a transfer coefficient often parameterized in terms of wind speed and surface roughness [*Arya*, 2001]. The BTM is applicable only when multiple-level gas concentration and wind speed data are available. Multiple-level observations of water vapor concentration (air humidity) are abundant while multiple-level measurements of other greenhouse gases such as CO_2 are less common from regional and global ground observation networks including AmeriFlux (http://ameriflux.lbl.gov/) and FLUXNET (http://fluxnet.fluxdata.org/).

The BTM is the only method for estimating gas fluxes in the Earth system models at regional and global scales. With the fast development of remote sensing technology, it is desirable if the gas fluxes at regional and global scales can be estimated using remote sensing observations. Yet, remote sensing observations of bulk gradient of gas concentration, wind speed and surface roughness as the inputs of a BTM are rarely available over the land surfaces. For example, bulk gradient data of gas concentration such as CO_2 are not available from the latest satellite Orbiting Carbon Observatory -3 (OCO-3) [*Basilio et al.*, 2019]. Remotely sensed surface wind over land does not exist [*Stoffelen et al.*, 2020]. Large scale remotely sensed land surface roughness is still to be validated [*Ullmann and Stauch*, 2020]. Therefore, an alternative method is needed for modeling gas fluxes over the land surfaces.

Non-gradient models (NGMs) of fluxes have been developed in the past two decades motivated by remote sensing applications. The first NGM is for ground heat flux using surface soil

temperature [*Wang and Bras*, 1999]. When heat conduction in soil layers follows a diffusive process, ground heat flux can be expressed as a functional of the time-history of surface soil temperature. The key idea behind the NGM of ground heat flux is that the spatial change of soil temperature (or temperature gradient) at a certain depth is linked to its temporal change at the same depth, through mathematical equations known as the half-order derivative/integral [*Hilfer*, 2000; *Miller and Ross*, 1993; *Nishimoto*, 1991; *Oldham and Spanier*, 2006; *Samko et al.*, 1993], when the soil temperature dynamics is described by a diffusion equation. The NGM of ground heat flux has been generalized to deriving soil heat flux (soil temperature) at any depth from surface temperature (ground heat flux) [*Wang*, 2012; *Yang and Wang*, 2014a; *Yang et al.*, 2017]. It is worth pointing out that the reverse problem, i.e. soil heat flux (soil temperature) at a deeper depth derived from surface soil temperature (ground heat flux), is ill-posed [*Beck et al.*, 1985]. Nonetheless, the concept of NGM provides new opportunities of remote sensing of hydrological fluxes. The NGM of ground heat flux has a unique advantageous feature of capturing phase shift between heat flux and temperature process. A comparison study[*Purdy et al.*, 2016] suggests that the NGM outperforms six commonly used models for simulating global ground heat flux due to its theoretical and technical strength. A recent study [*Gao et al.*, 2017] on comparison of nine models of soil heat flux has shown that the NGM is the only one with no modeling error of phase. The NGMs of heat fluxes have been applied to a variety of topics in geosciences including hydrology, meteorology, climatology, geophysics, glaciology, etc. [*Beltrami et al.*, 2000; *Bennett et al.*, 2008; *Hsieh et al.*, 2009; *Yang et al.*, 2020; *Zhu et al.*, 2014].

The NGMs of mass fluxes have also been proposed and tested. When the transport of salt in the top ocean layer is dominated by a one-dimensional (vertical) diffusion process with a time-variable diffusivity, the salt flux at the sea surface can be expressed as integrated time function of

sea surface salinity similar to the formula of the NGM of soil heat flux [*Nieves et al.*, 2014]. This NGM of salinity leads to the first salinity-based model of ocean surface fresh water flux (e.g. evaporation) taking advantage of the recently available more abundant satellite observations of sea surface salinity. These previous theoretical and modeling studies have laid foundation for more applications of the non-gradient method to modeling mass and energy fluxes of the Earth system.

The goal of this study is to formulate and test new NGMs of gas fluxes over the land surfaces. A major challenge is to parameterize the variable eddy-diffusivity characterizing boundary layer turbulence in the governing equation of gas transfer. Thanks to a new parameterization of eddy-diffusivity of the boundary-layer turbulence [*Wang and Bras*, 2010], an analytical solution has been derived to express a gas flux as an integrated time function of single-level gas concentration record analogous to the soil heat flux – soil temperature relationship.

2. Model Formulation

The dynamics of a non-reactive gas concentration within the atmospheric surface layer is often described by a one-dimensional diffusion equation when turbulent mass transport is predominantly vertical [*Nieuwstadt*, 1980],

$$\frac{\partial C}{\partial \mathrm{t}} = \frac{\partial}{\partial \mathrm{z}}\left[D_c(z,t)\frac{\partial C}{\partial \mathrm{z}} \right] \tag{1}$$

where C (kg m^{-3}) is the (temporal) mean gas concentration, $D_c(z, t)$ (m^2 s^{-1}) the turbulent eddy-diffusivity, z (m) the distance above the ground or canopy, and t (s) the time. D_c is usually parameterized based on the Monin-Obukhov similarity theory (MOST) of the boundary layer turbulence (e.g. [*Arya*, 2001]) assuming that the turbulent flow responsible for heat transfer is also responsible for the transport of passive tracers such as water vapor and CO_2 [*Monteith and*

Unsworth, 2013]. In this study, a new parameterization of D_c is used based on the extreme solution (ES) of the equations of MOST (Appendix A) [*Wang and Bras*, 2010],

$$D_c(z,t) = D_0 z^{\frac{4}{3}} |H(t)|^{\frac{1}{3}}, \tag{2}$$

where H (W m^{-2}) is sensible heat flux (defined as positive when heat is transferred from the land surface into the atmosphere) and D_0 an empirical constant depending on the atmospheric stability given in Eq. (A4). The ES covers all regimes of forced convection, free convection, and anything in-between. It allows D_c to be formulated as functions of friction velocity u_*, sensible heat flux H, (mean) wind shear or (mean) temperature gradient (see Table 1 of [*Wang and Bras*, 2010]). Therefore, D_c expressed in terms of u_* does not necessarily imply that the stratification is neutral. The ES-based D_c has different values for day and night times corresponding to unstable and stable condition (Eqs. (A1) – (A4)), respectively.

It can be shown (Appendix A) that gas flux F, defined as positive into the atmosphere, is expressed as,

$$\begin{aligned} F(z,t) &\equiv -D_c(z,t)\frac{\partial C}{\partial z} \\ &= \frac{D_c(z,t)}{\sqrt{\pi}} \int_0^t \frac{\partial C(z,\tau)}{\partial \tau} \left[\int_\tau^t D_c(z,\zeta)\, d\zeta \right]^{-\frac{1}{2}} d\tau \end{aligned}, \tag{3}$$

where τ, ζ are the integration (dummy) variables. Eq. (3) holds for the specific parameterization of D_c as in Eq. (2). For the case of constant D_c, Eq. (3) reduces to

$$F(z,t) = \sqrt{\frac{D_c}{\pi}} \int_0^t \frac{\partial C(z,\tau)}{\partial \tau} \frac{d\tau}{\sqrt{t-\tau}}, \tag{4}$$

which is recognized as the half-order (time) derivative of $C(z,t)$, identical to the NGM of soil heat flux [*Wang and Bras*, 1999]. Eq. (3) involves a singular integrand with a removable singularity at $\tau = t$. A numerical integration algorithm for computing F is given in Appendix B.

Eq. (3) shows that F at a given time t can be derived from the time-history of $C(z,t)$ from an initial time (τ=0) to the current time (τ=t). Theoretically, $F = 0$ at the initial time of the integral corresponding to uniform profile of C. A sensitivity test (Figure A2 in Appendix A) indicates that F is not sensitive to the initial condition of C as long as the integration period is ~ 24 hours for simulating diurnal variations of F since the weighting function in the integrand decays rapidly with time (Figure B2 in Appendix B). Note that Eq. (3) predicts F over the entire period (0 to t) given the data of C and H (for parameterizing D_c) over the same period.

Eqs. (1) - (3) hold for a certain range of z within the surface layer. Since F and H are nearly uniform in the surface layer [*Stull*, 1988], F as in Eq. (3) represents the "surface" flux. z in Eq. (3) for the case of forest is approximately the distance between the canopy top and the eddy-covariance (EC) fluxes measurement height. For the case of shorter vegetation such as grasslands and croplands, z is chosen as ~ 5 m instead of the measurement height [*Cellier*, 1986] since the MOST is valid above a height ~ 2-5 times of the height of the roughness elements [*Basu and Lacser*, 2017]. Note that the effect of the uncertainty of z on the NGM gas flux is relatively weak due to its $z^{\frac{2}{3}}$-dependence according to Eq. (3). Therefore, the NGM of gas fluxes is not sensitive to this parameterization of eddy-diffusivity.

Figure 1 compares the NGM fluxes of water vapor (F_v) and CO_2 (F_c) according to Eqs. (3) and (4) using hourly data during a ten-day period at the BR-Sa1 site (site description in Table 1). $D_c(z,t)$) changes from 2 (nighttime) to 16 $m^2 s^{-1}$ (daytime) with an average value of 6.18 $m^2 s^{-1}$

(Figure A1 in Appendix A). It is evident that both NGMs are capable of capturing the magnitude and diurnal variations of the observed fluxes, and the NGM with the time-variable $D_c(z,t)$ performs better than the NGM with a constant diffusivity parameter. The diurnal cycles of the NGM fluxes are dominated by those of gas concentrations.

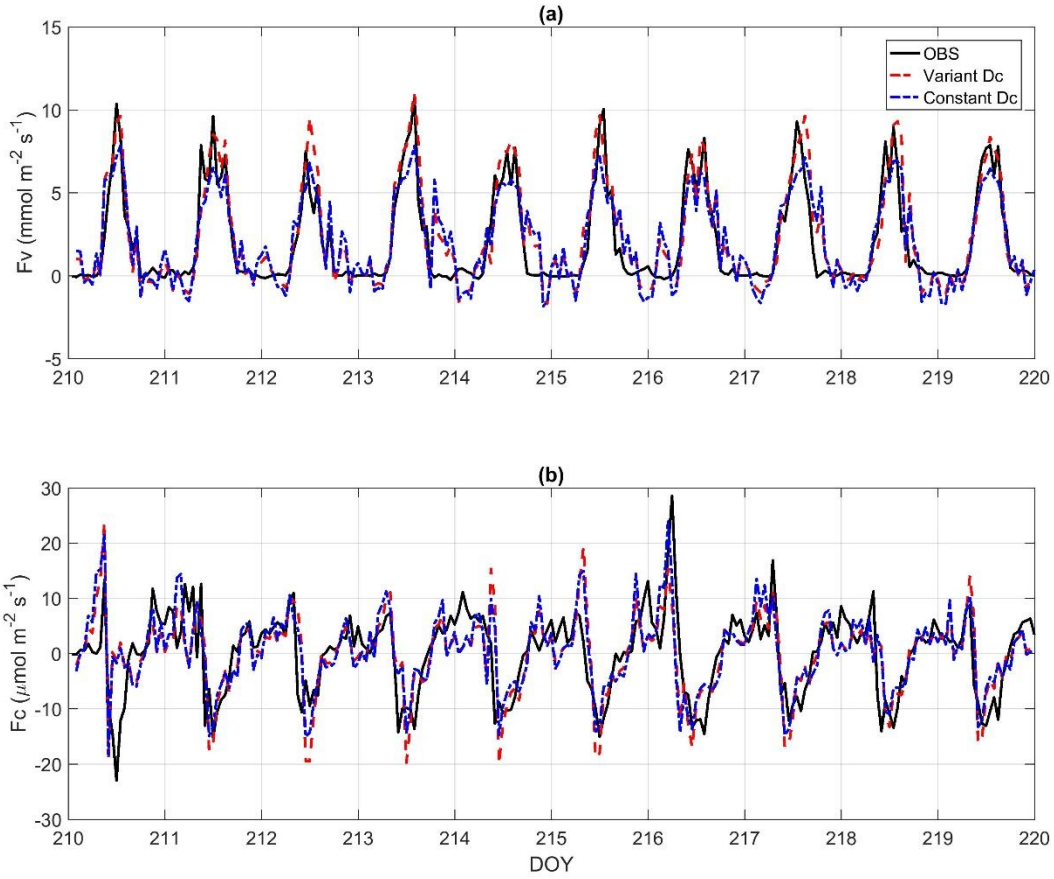

Figure 1. The NGM F using variable $D_c(z,t)$ vs. constant D_c compared with observed F (OBS) **(a)** water vapor flux (F_v) and **(b)** CO_2 flux (F_c) at the BR-Sa1 site, Jul. 29- Aug. 8, 2003

The proposed NGM of gas fluxes has several advantageous properties resulting, in part, from the new parameterization of eddy-diffusivity. Obviously, modeling gas fluxes without using gas concentration gradient data is the most attractive feature of the NGM. Reduced sensitivity of

the NGM to the parameterization of eddy-diffusivity leads to more robust estimates of gas fluxes since the parameterization of eddy-diffusivity is subject to substantial uncertainty [*Gopalakrishnan et al.*, 2013]. Compared to the eddy-diffusivity formula based on the classical formulation of the equations of MOST, the extremum solution provides a parameter parsimonious formula of eddy-diffusivity mathematically independent of surface wind speed (or friction velocity) and surface roughness. Not using canopy and aerodynamic conductance (or resistance) parameter in the NGM formulation leads to reduced modeling errors compared to the bulk flux models. The above advantages of the NGM facilitate modeling regional and global analysis as remote sensing observations and reanalysis products of the model inputs (i.e. CO_2 concentration for carbon flux, relative humidity for evapotranspiration, and net radiation for sensible heat flux) are becoming more abundant with improved quality[*Basilio et al.*, 2019; *Ramírez- Beltrán et al.*, 2019; *Verma et al.*, 2016].

D_c in Eq. (2) based on the extremum solution can be formulated in terms of one of the four variables, i.e. sensible heat flux, friction velocity, temperature gradient, and wind shear [*Wang and Bras*, 2010]. For the purpose of developing a NGM of gas fluxes, sensible heat flux and friction velocity are two viable options. Since friction velocity is difficult to measure or model using remote sensing observations, H is the obvious choice in the parameterization of D_c. Although H cannot be directly measured remotely and in-situ measurement of H using EC method is costly, the maximum entropy production (MEP) model [*Wang and Bras*, 2011] is an attractive approach for modeling H (and latent heat/water vapor flux E) using field and remote sensing meteorological data. The MEP model itself is a non-gradient model of surface heat fluxes, a feature consistent with the proposed NGMs of gas fluxes. The theoretical basis and mathematical formulation of the

MEP model have been published previously [*Wang and Bras*, 2009; 2011; *Wang et al.*, 2014]. A brief overview of the MEP model is given in Appendix C.

For the case of dense canopy related to this study, the MEP model of H (and E) is formulated as,

$$H = \frac{R_n}{1+B(\sigma)}, \quad E = \frac{R_n}{1+B^{-1}(\sigma)}$$
$$B(\sigma) = 6\left(\sqrt{1+\frac{11}{36}\sigma}-1\right), \qquad \sigma = \frac{\lambda^2}{c_p R_v}\frac{q_s}{T_s^2}, \tag{5}$$

where R_n (W m^{-2}) is net radiation, T_s (K) canopy surface temperature, and q_s (kg kg^{-1}) canopy surface (specific) humidity. Other physical parameters include latent heat of vaporization of liquid water λ (2.5×10^6 J kg^{-1}), gas constant of water vapor R_v (461 J kg^{-1} K^{-1}), and specific heat of air at constant pressure c_p (10^3 J kg^{-1} K^{-1}). $B(\sigma)$ is the reciprocal Bowen ratio expressed as an analytical function of a dimensionless parameter σ representing the relative role of surface water and thermal condition on the partition of R_n into E and H. Note that $B(\sigma)$ is calculated from the MEP formulation and not a predefined Bowen ratio. Extensive tests of the MEP model from local to global scales have been reported previously [*Wang and Bras*, 2009; 2011; *Nearing et al.*, 2012; *Wang et al.*, 2014; *Yang and Wang*, 2014b; *Shanafield et al.*, 2015; *Huang et al.*, 2016; *Wang et al.*, 2017; *Hajji et al.*, 2018; *El Sharif et al.*, 2019; *Li et al.*, 2019; *Xu et al.*, 2019]. Since the MEP modeled H is constrained by surface energy balance, the NGM of gas fluxes is implicitly energy balance constrained, another advantageous feature of the NGMs.

3. Data

The NGMs as in Eqs. (2) – (3) are tested using field observations of water vapor and CO_2 concentration and the corresponding EC fluxes. H in Eq. (2) is estimated using the MEP model

with field observations of net radiation, surface temperature and humidity. The MEP modeled *H* is validated against the EC flux measurements (Figure S1 in the Supporting Information (SI)).

3.1 Test Sites

Six test sites, mostly from the AmeriFlux network, with diverse climates, geography, and vegetation types (Table 1) are selected to evaluate the performance of the proposed NGM. The sites include rainforest, mid-latitude forest, cropland, grassland, and wetland from 3 °S to 45 °N with high water vapor and CO_2 fluxes. Growing season data with minimum data gaps are selected for testing the NGM at diurnal scale at all sites. Tests of the NGM at seasonal scale use data at BR-Sa1 and US-MRf with high data availability percentage, the ratio of available data points to the total data points. The available percentages of CO_2 concentration, CO_2 fluxes, and water vapor (latent heat) fluxes at BR-Sa1 in 2003 are 93 %, 88 %, and 88 %, respectively; and those at US-MRf in 2007 are 94 %, 77 %, and 84 %, respectively.

3.2 Quality of EC fluxes data

EC fluxes are subject to measurement uncertainty caused by sampling frequency, uncertainty of the mean variables, and instrument calibration errors among others [*Aubinet et al.*, 2012]. The EC measurement errors vary with land covers and increase with the magnitude of fluxes. The measurement errors over forest are generally larger than over grassland or cropland [*Richardson et al.*, 2006]. Daytime relative flux uncertainty, the ratio of standard deviation of random errors to hourly mean, is ~20% at maize site and ~40% at forest site [*Vickers et al.*, 2010]. Nighttime EC fluxes are more uncertain than daytime fluxes due to intermittency of turbulence, low wind speed, and temperature inversion [*Aubinet*, 2008; *Baldocchi*, 2003]. At forest sites, the relative uncertainty of EC water vapor fluxes could reach 80% during nighttime compared to 40% during daytime [*Vickers et al.*, 2010]. Hence, nighttime fluxes are often rejected for the analysis

of model simulations [*Barr et al.*, 2006]. The EC fluxes during winters are more uncertain than during summers due to weak turbulence, strong stability, and liquid water in gas analyzer path [*Post et al.*, 2015]. EC fluxes during rainy periods are especially problematic caused by instrument malfunction. Raindrops and ice may block the transducer path and attenuate the ultrasonic signals of sonic anemometer, leading to degraded three-dimensional wind speed measurements [*Aubinet et al.*, 2012]. Water drops on the sapphire windows of infrared gas analyzer head can weaken sensor signals, leading to unrealistic gas concentration readings. In this study, growing season data excluding rainy periods are used for the model tests at diurnal scale as suggested [*Hollinger and Richardson*, 2005; *Wilson et al.*, 2001] (Precipitation data in Figure S3 of SI).

Table 1. Site Information

Site id	Lat, Lon	IGBP	Climate	T_a (°C)	P (mm)	z_c (m)	z_m (m)	TR (min)	DOI	Reference
BR-Sa1	2.9 °S, 55.0 °W	EBF	Am	26	2,075	45	58	60	10.17190/AMF/1245994	[*Saleska et al.*, 2003]
US-MRf	44.6 °N, 123.6 °W	ENF	Csb	10.2	1,819	30	38.3	30	10.17190/AMF/1246049	[*Thomas et al.*, 2013]
CCZO	34.6 °N, 81.7 °W	ENF	Cfa	16	1,300	6	9	30		
US-Br3	42.0 °N, 93.7 °W	CRO	Dfa	8.9	847	-	2.4	30	10.17190/AMF/1246039	[*Dold et al.*, 2017]
US-IB2	41.8 °N, 88.2 °W	GRA	Dfa	9	930	-	3.8	30	10.17190/AMF/1246066	[*Miller et al.*, 2002]
US-ORv	40.0 °N, 83.0 °W	WET	Cfa	11.6	1,499	-	9.6	30	10.17190/AMF/1246135	[*Morin et al.*, 2017]

Note. IGBP: EBF (evergreen broadleaf rainforest), ENF (evergreen needleleaf forest), CRO (cropland), GRA (grassland), WET (permanent wetland). Climate: Am (tropical monsoon), Csb (Mediterranean), Cfa (humid subtropical), Dfa (humid continental). T_a: annual mean temperature. P: annual mean precipitation. z_c: canopy height. z_m: EC measurement height. TR: time resolution.

4. Test Results

4.1 Water vapor fluxes

4.1.1 Diurnal scale analysis

The canopy (leaf) surface water vapor concentration (C_v) (absolute humidity) is approximated as the water vapor concentration in the air since C_v is rarely measured in field experiments. Water vapor concentration can be calculated from air temperature T_a and relative humidity *RH* using the Clausius-Clapeyron equation. Such calculated C_v leads to the close agreement of the modeled (NGM) and observed (OBS) water vapor fluxes (F_v) at all test sites. *H* in D_c (Eq. (2)) is calculated from net radiation R_n, T_a, and/or *RH* using the MEP model. Note that the NGM fluxes are not sensitive to D_c and constant D_c is able to capture the magnitude and phase of the fluxes as demonstrated in Figure 1. Nonetheless, D_c calculated using the MEP and OBS *H* agree closely (Figure S2 in SI). The test statistics including rooted-mean-square-errors (RMSE), normalized RMSEs or NRMSE (RMSE divided by the range of the OBS fluxes), and correlation coefficients (*r*) of the NGM vs. OBS F_v are summarized in Table 2. The NGM accurately captures the magnitude, phase, and diurnal variation of F_v at all sites (Figure 2) given ~ 20% uncertainty of the EC measurements for cropland and forest [*Vickers et al.*, 2010]. The NGM and OBS F_v agree more closely during daytime than nighttime. The NGM F_v is unrealistic (e.g. DOY 184 in Figure 5(d) and DOY 165 in Figure 5(e)) when C_v has spurious fluctuations due to precipitation or sudden changes of *RH* or T_a (Figures S3 to S5 in the SI). The NGM well captures the diurnal cycles of F_v at all test sites. *r*s of the NGM vs. OBS F_v are high (≥0.82).

Table 2. Statistics of NGM vs. OBS F_v and F_c in diurnal scale analysis: RMSE, NRMSE, *r*

	F_v (mmol m^{-2} s^{-1})			F_c (μmol m^{-2} s^{-1})		
Site ID	RMSE	NRMSE	*r*	RMSE	NRMSE	*r*
BR-Sa1	1.35	12%	0.9	6.02	12%	0.66
US-MRf	0.83	13%	0.87	7.49	18%	0.80
CCZO	1.00	7%	0.88	7.98	17%	0.89
US-Br3	0.80	10%	0.94	6.18	19%	0.64
US-IB2	2.05	16%	0.86	17.77	25%	0.58
US-ORv	2.22	11%	0.82	7.36	10%	0.47

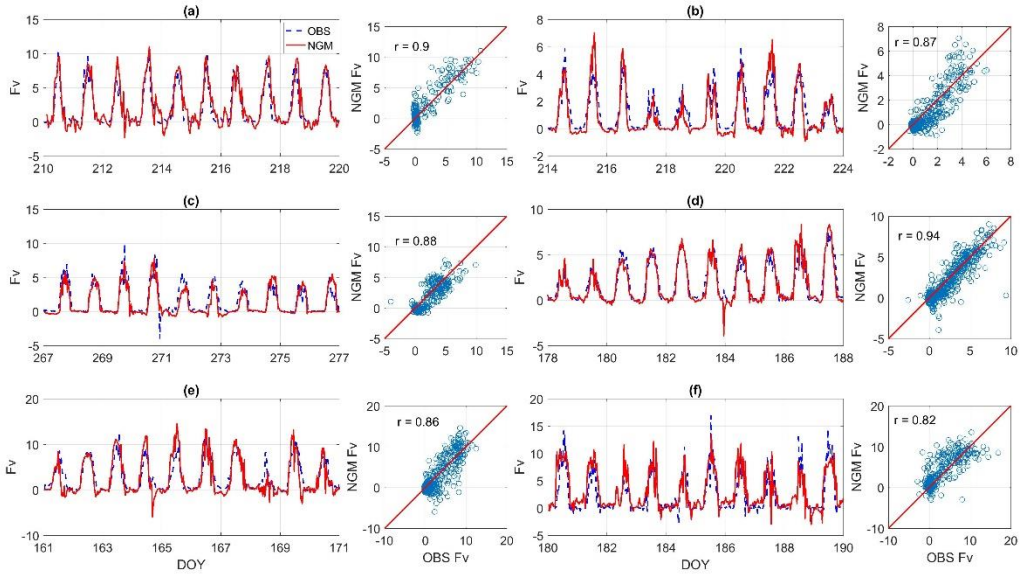

Figure 2. NGM and OBS F_v (mmol m^{-2} s^{-1}) at **(a)** BR-Sa1, Jul. 29- Aug. 8, 2003, **(b)** US-MRf, Aug. 2- Aug. 12, 2007, **(c)** CCZO, Sep. 24- Oct. 4, 2017, **(d)** US-Br3, Jun. 27- Jul. 7, 2007, **(e)** US-IB2, Jun. 9 - Jun. 19, 2006, and **(f)** US-ORv, Jun. 29 - Jul. 9, 2011

4.1.2 Seasonal scale analysis

The NGM is tested at seasonal scale using data at BR-Sa1 in 2003 and US-MRf in 2007 when the available percentages of hourly CO_2 concentration, CO_2 fluxes, and water vapor (latent heat) fluxes at BR-Sa1 in 2003 are 93 %, 88 %, and 88 %, respectively; and those at US-MRf in 2007 are 94 %, 77 %, and 84 %, respectively. Hourly/half-hourly inputs are used to calculate hourly/half-hourly F_v and thereafter monthly accumulations and diurnal means at both sites. Panels (a) in Figures 3 and 4 show the monthly accumulative daytime (^{DT}, 6 AM to 6 PM), nighttime (^{NT}, 6 PM to 6 AM), and all-day NGM and OBS F_v. Panels (b) and (c) compare the monthly diurnal mean of NGM and OBS F_v. Panels (d) and (e) compare the annual diurnal mean of NGM and OBS F_v. The statistics of the diurnal means are summarized in Table 3. The annual fluxes and relative errors σ (the ratio of absolute error to the magnitude of the OBS flux) of annual F_v are given in Table 4.

Table 3. Statistics of NGM vs. OBS F_v and F_c in seasonal scale analysis: RMSE, NRMSE, r

F_v (mmol m^{-2} s^{-1})						
Site ID	RMSE[a]	NRMSE[a]	r^a	RMSE[b]	NRMSE[b]	r^b
BR-Sa1	0.63	7%	0.97	0.34	5%	0.99
US-MRf	0.43	10%	0.95	0.32	12%	0.97
F_c (μmol m^{-2} s^{-1})						
BR-Sa1	3.9	14%	0.89	2.33	10%	0.96
US-MRf	4.34	19%	0.9	3.1	18%	0.99

[a] monthly diurnal mean, [b] annual diurnal mean.

Table 4. Statistics of annual F_v and F_c

F_v (mm year^{-1})									
	Daytime			Nighttime			All-Day		
Site ID	NGM	OBS	σ	NGM	OBS	σ	NGM	OBS	σ
BR-Sa1	1129	1067	6%	16	28	42%	1145	1095	5%
US-MRf	418	481	13%	-15	38	138%	404	519	22%
F_c (gC m^{-2} year^{-1})									
	Daytime			Nighttime			All-Day		
Site ID	NGM	OBS	σ	NGM	OBS	σ	NGM	OBS	σ
BR-Sa1	-1199	-1280	6%	922	920	0.28%	-277	-361	23%
US-MRf	-1681	-1898	11%	912	229	297%	-769	-1669	54%

The NGM accurately simulates the monthly F_v at BR-Sa1 (Figure 3 (a)). Both the magnitudes and variations of the monthly daytime NGM and OBS F_v are in good agreement. The monthly nighttime NGM and OBS F_v almost overlap throughout the year. The annual daytime NGM and OBS F_v are 1129 and 1067 mm, respectively, with σ 6%. Both the OBS and NGM annual nighttime F_v are close to zero. The NGM annual F_v is accurate with σ only 5%. The annual NGM flux (evapotranspiration ET, 1145 mm with annual precipitation 1920 mm) at BR-Sa1 for 2003 is also consistent with the reported ET (1281 mm with precipitation 2200 mm for 2001) at a site 23 km from BR-Sa1 [*da Rocha et al.*, 2004]. The monthly and annual diurnal mean of the NGM and OBS F_v are in close agreement (Figures 3 (b) to (e)) with NRMSEs below 7% and rs > 0.97. The statistics at BR-Sa1 suggest that the NGM performs well at seasonal scale.

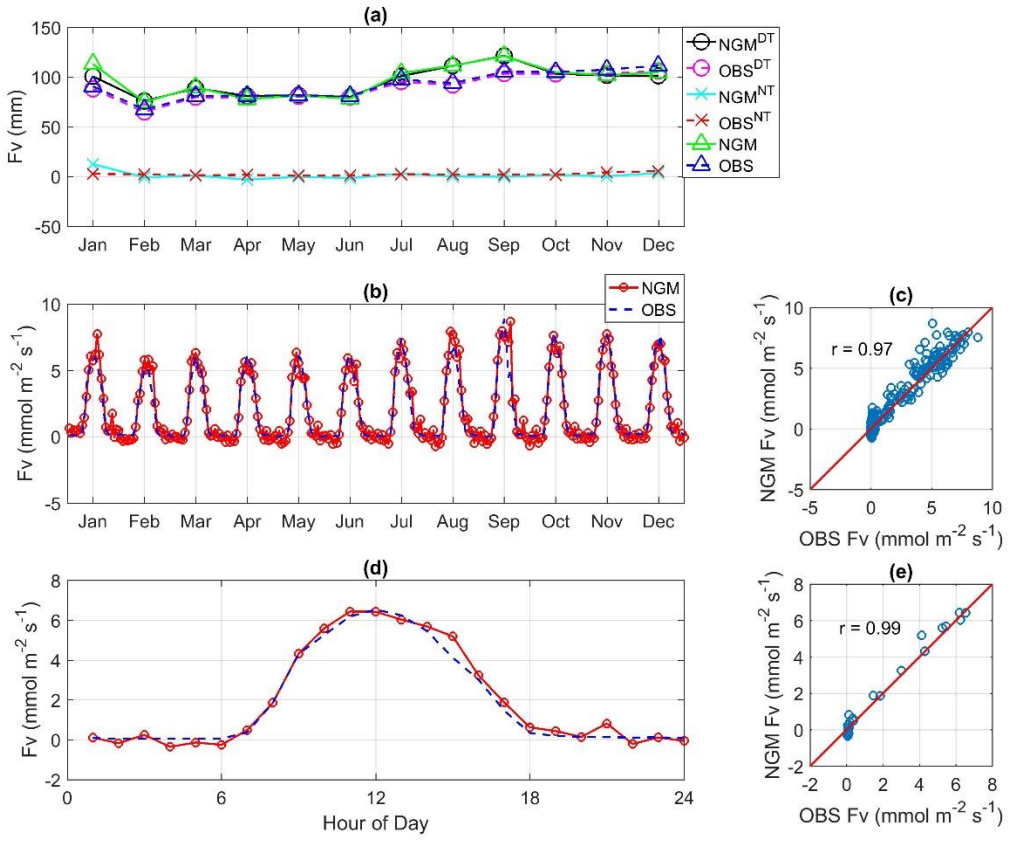

Figure 3. (**a**) Monthly accumulations, (**b**) and (**c**) monthly diurnal mean, and (**d**) and **(e)** annual diurnal mean of NGM and OBS F_v at BR-Sa1, 2003

The NGM captures the seasonal magnitudes and phases of the monthly daytime and all-day F_v (Figure 4(a)) at US-MRf, an evergreen needleleaf forest in the mid-latitudes. The monthly daytime NGM and OBS F_v reach July maxima and December minima. The monthly nighttime NGM and OBS F_v are nearly zero throughout the year. The annual daytime NGM and OBS F_v are 418 and 481 mm, respectively, with σ 13% (Table 4). The annual nighttime NGM and OBS F_v are almost zero. The negative F_v estimated using the NGM is more reasonable than the positive OBS F_v given condensation and negative net radiation at nighttime. The annual NGM ET is consistent with site-published ET (478 mm, http://terraweb.forestry.oregonstate.edu/marys-river-fir-

ameriflux-site-us-mrf) at US-MRf and the observed ET (415 mm) at a nearby site [*Anthoni et al.*, 1999]. It is evident that the NGM well captures the monthly and annual diurnal mean of the OBS F_v with NRMSEs < 12% and *r*s > 0.95 (Figures 4(b) to (e)). The seasonal tests demonstrate that the NGM is capable of modeling seasonality of ET over mid-latitude forests.

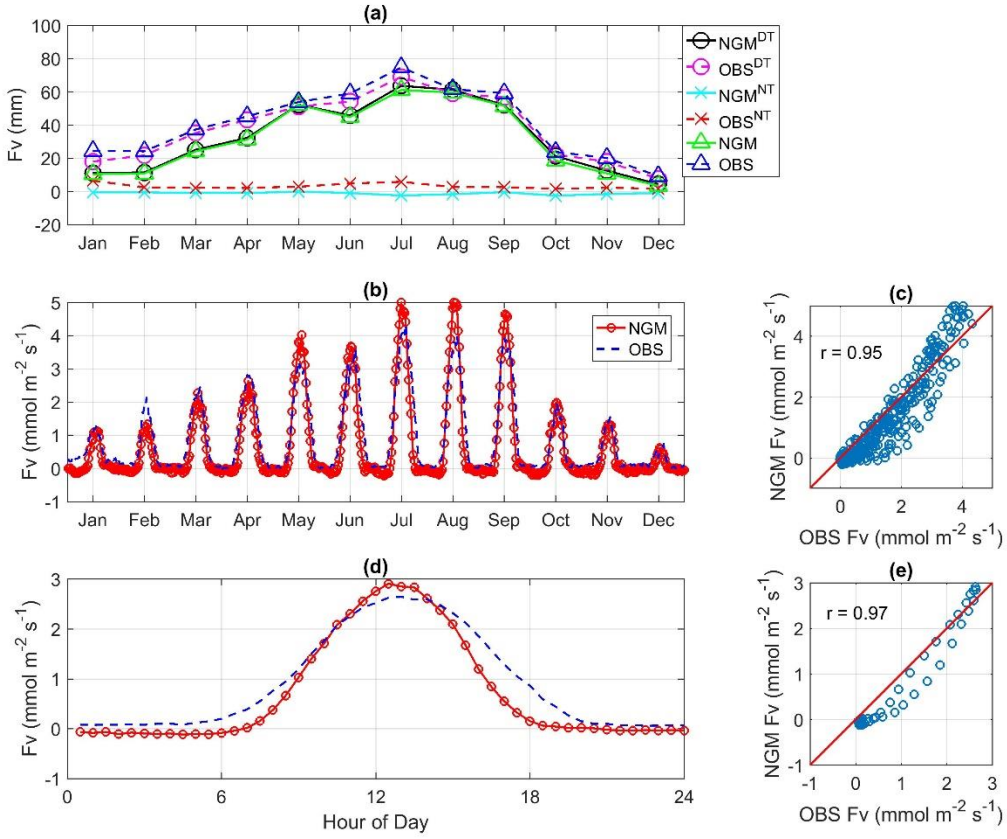

Figure 4. (**a**) Monthly accumulations, **(b)** and (**c**) monthly diurnal mean, and (**d**) and **(e)** annual diurnal mean of NGM and OBS F_v at US-MRf, 2007

4.2 CO_2 fluxes

4.2.1 Diurnal scale analysis

The NGM performs equally well for modeling CO_2 fluxes. It accurately simulates the daytime F_c (Figure 5) measured by the same statistics as those of the NGM F_v (Table 2). The

nighttime NGM F_c appears to be more realistic than the observed ones as the EC system tends to underestimate the nighttime CO_2 fluxes in the stably stratified atmosphere [*Aubinet*, 2008; *Baldocchi*, 2003; *Falge et al.*, 2001; *Goulden et al.*, 1996; *Gu et al.*, 2005; *Hollinger and Richardson*, 2005]. The NGM captures the large positive F_c in the early mornings over forests (Figure 5 (a)), presumably caused by the quick release of night time CO_2 storage [*Nicolini et al.*, 2018]. The discrepancies between the NGM and OBS F_c in the early mornings become larger (DOY 215 in (b), DOY 270 in (c), DOY 186 in (d), DOY 164 in (e), and DOY 181 in (f) of Figure 6) when the measured CO_2 concentration has spurious fluctuations (i.e. > 450 ppm (Figure S7 in SI) since CO_2 concentration above active vegetation cannot be higher than 450 ppm [*Franks et al.*, 2014]. Unrealistically large CO_2 concentration during rain events (Figure S3 in the SI) has the same effect on the NGM F_c on DOY 164, 168, and 171 (Figure 5(e)). Dew and rain are the leading causes of the measurement errors of CO_2 concentration by the open-path gas analyzers during the test periods [*Aubinet et al.*, 2012]. The unrealistically large time change rates of CO_2 concentration lead to erroneous nighttime NGM F_c (e.g. > 20 μmol m^{-2} s^{-1} hourly change). Yet the measurement errors of CO_2 concentration have limited influence on the NGM fluxes as a result of the rapid decaying of the D_c -dependent integration kernel. The NGM performs well in simulating diurnal cycle of F_c.

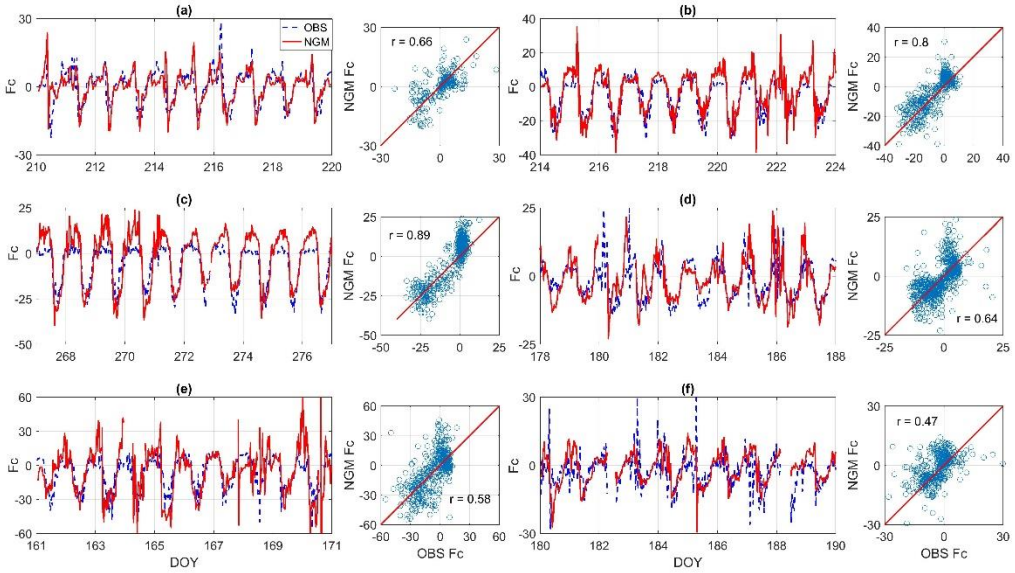

Figure 5. NGM and OBS F_c (μmol m^{-2} s^{-1}) at **(a)** BR-Sa1, Jul. 29- Aug. 8, 2003, **(b)** US-MRf, Aug. 2- Aug. 12, 2007, **(c)** CCZO, Sep. 24- Oct. 4, 2017, **(d)** US-Br3, Jun. 27- Jul. 7, 2007, **(e)** US-IB2, Jun. 9 - Jun. 19, 2006, and **(f)** US-ORv, Jun. 29 - Jul. 9, 2011

4.2.2 Seasonal scale analysis

The NGM of F_c is tested at seasonal scale using hourly/half-hourly input data at BR-Sa1 and US-MRf (Figures 6 and 7) with the corresponding statistics in Table 3. The monthly NGM and OBS F_c at BR-Sa1 are in good agreement (r ~ 0.9) (Figure 6 (a)) that is closer for dry months (June to September) than wet months (November to January) due to higher measurement errors of CO_2 concentration in rainy season (page 77 in [*Burba*, 2013]) as discussed previously. The annual mean diurnal cycles of the NGM and OBS F_c (Figure 6(d)) agree more closely (r ~ 0.96).

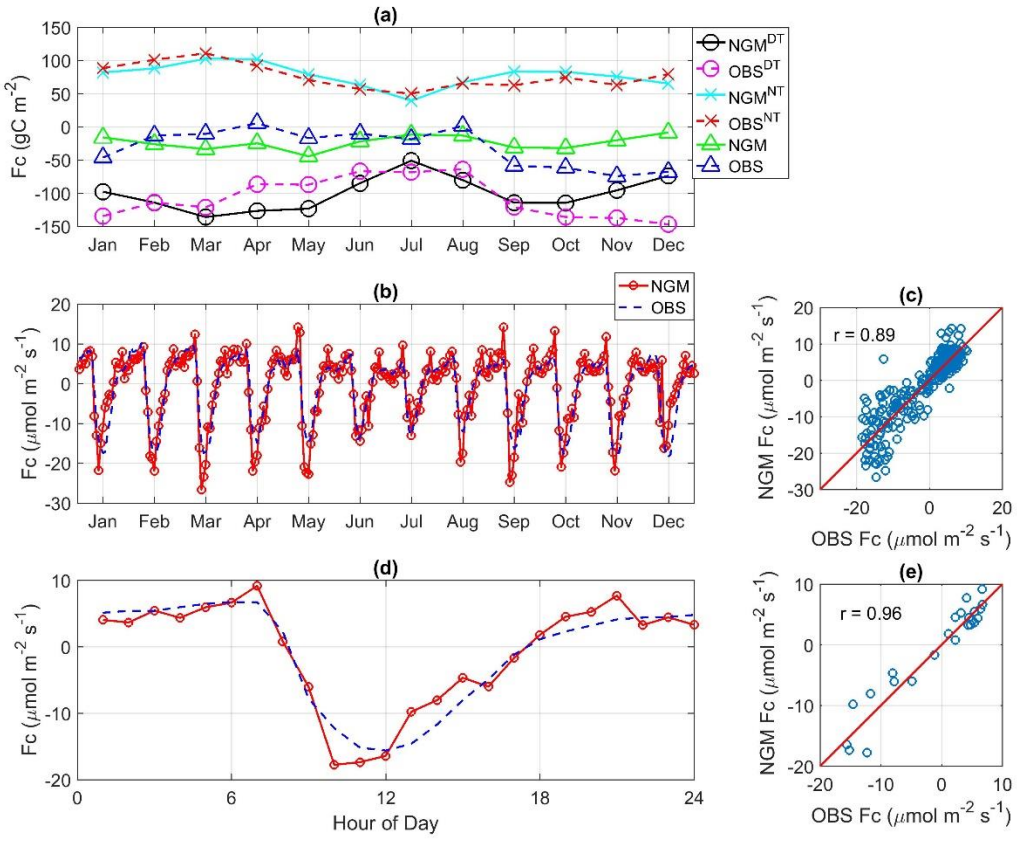

Figure 6. (**a**) Monthly accumulations, (**b**) and **(c)** monthly diurnal mean, and (**d**) and **(e)** annual diurnal mean of NGM and OBS F_c at BR-Sa1, 2003.

Numerous efforts over the past decades have been made to assess the Amazon carbon budgets, seeking answers to the question whether the Amazon rainforest is a carbon source or sink [*Brienen et al.*, 2015; *Gatti et al.*, 2014; *Phillips et al.*, 2009; *Saleska et al.*, 2003; *Tian et al.*, 1998]. The uncertainties in the current CO_2 fluxes data are arguably responsible for the unbalanced carbon budget at regional and global scales, causing the missing carbon sink problem [*Schimel*, 1995]. Previous analysis of EC data at BR-Sa1 from 2001 to 2003 [*Saleska et al.*, 2003] suggested that the Amazon forest has changed from a carbon sink to a carbon source when more than 50 % of nighttime EC flux data are rejected based on a threshold of friction velocity. Short data gaps are

filled by linear interpolation and long gaps by the mean (good) nighttime flux (details in the Supporting Online Material for [*Saleska et al.*, 2003]). In this study, the NGM uses more than 90 % of the CO_2 data to simulate F_c with the gaps filled by mean values at the same hour of day. More than 88 % of the EC CO_2 flux data are used to compute the annual diurnal mean and accumulative fluxes for 2003. The annual accumulative daytime NGM and OBS F_c at BR-Sa1 are -1199 and -1280 gC m^{-2}, respectively, with σ 6 %. The annual accumulative nighttime NGM and OBS F_c are 922 and 920 gC m^{-2}, respectively, with σ 0.3 %. The NGM estimate of the net ecosystem exchange (NEE) (annual accumulative all-day F_c in Table 3) at BR-Sa1 is -277 gC m^{-2}, indicating that the rainforest at BR-Sa1 is a carbon sink for 2003. This finding is consistent with a recent study based on the field biometric data collected at 321 locations across mature forest from 1983 to 2011 [*Brienen et al.*, 2015]. The NGM is shown to be a promising new modeling tool for the assessment of the Amazon carbon budgets at diurnal and seasonal scales.

The NGM captures accurately the seasonality of the monthly accumulative daytime F_c at US-MRf (Figure 7). The annual accumulative daytime NGM and OBS F_c, -1681 and -1898 gC m^{-2},respectively, with σ 11 % are within the range of 45 % uncertainty of daytime F_c measurements at the nearby mature pine site [*Vickers et al.*, 2010]. The monthly mean diurnal cycles of the NGM and OBS F_c are in good agreement except for rainy periods in June 2007 (Figure S8 in SI) when 15% of the EC CO_2 data are missing. The annual diurnal means of the NGM and OBS F_c agree more closely during daytime than nighttime. Underestimation of nighttime F_c by the above-canopy EC system at this site was reported [*Thomas et al.*, 2013]. A below-canopy EC system was used to obtain more accurate estimates of NEE [*Thomas et al.*, 2008]. The NGM nighttime F_c is almost zero μmol m^{-2} s^{-1} during the (low temperature) winter and reaches 10 μmol m^{-2} s^{-1} during the (high temperature) summer, consistent with the nighttime ecosystem respiration calculated using above-

and below-canopy EC systems [*Thomas et al.*, 2013]. The annual NGM NEE (-768 gC m^{-2} $year^{-1}$) in 2007 is also consistent with the NEE (-563 gC m^{-2} $year^{-1}$) calculated from two-level EC fluxes, supposedly more accurate than the NEE (-1258 gC m^{-2} $year^{-1}$) calculated from above-canopy EC fluxes [*Thomas et al.*, 2013]. The NGM provides a new opportunity for improving the assessment of carbon budgets over the mid-latitude forest given that only limited field sites provide profile data of CO_2 concentration and flux.

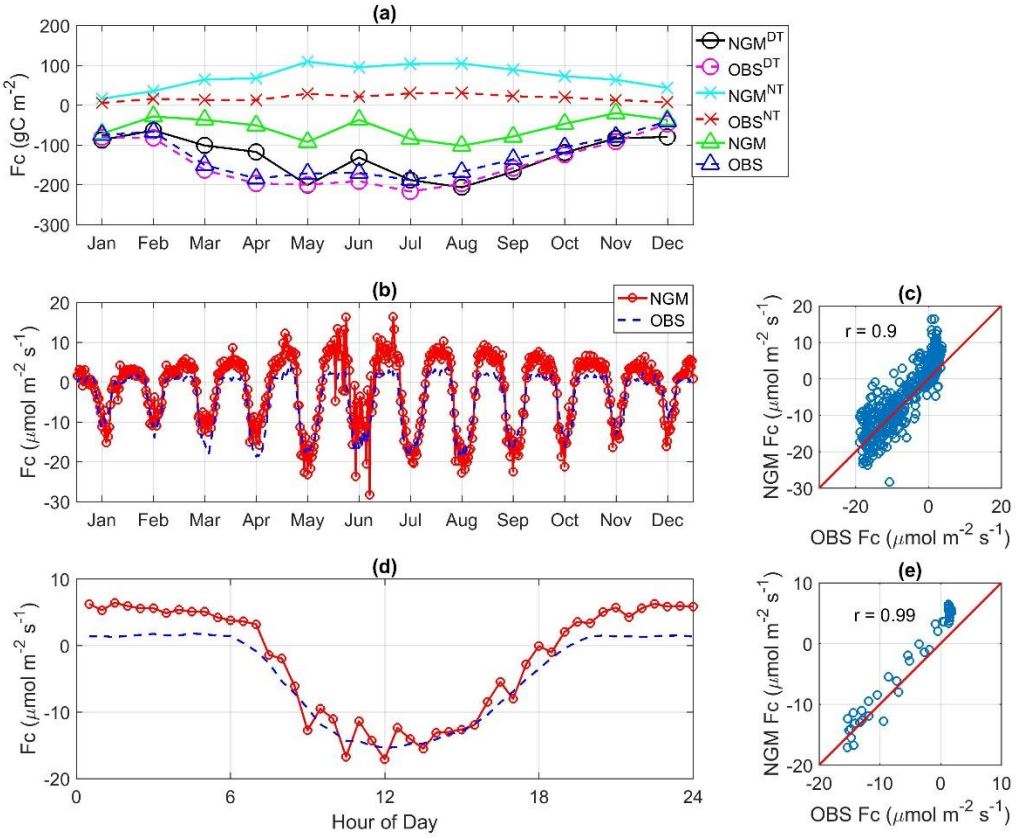

Figure 7. (**a**) Monthly accumulations, (**b**) and (**c**) monthly mean diurnal cycles, (**d**) and **(e)** annual mean diurnal cycles of NGM and OBS F_c at US-MRf, 2007

4.3 Methane fluxes

A preliminary test of the NGM of methane flux (FCH_4) uses methane concentration (CH_4) data collected at a peatland pasture site (US-Snd), California, United States (38.04 °N, 121.75 °W)

[*Hatala et al.*, 2012] (Figure 8). The canopy height is ~ 0.3 m during summer. The climate is Mediterranean with annual mean temperature 16°*C* and precipitation 358 mm. Half-hourly EC fluxes and other meteorological variables were measured at ~ 3 m above the ground. The NGM and OBS FCH_4 are in reasonable agreement given that the relatively large uncertainty of the EC FCH_4 flux data (20 - 300 % [*Kroon et al.*, 2010]. The NGM captures an event of large FCH_4 flux corresponding to a rapid increase of CH_4 concentration on DOY 120. The RMSE, NRMSE, and *r* of the NGM vs. OBS FCH_4 are 41 nmol m^{-2} s^{-1}, 14 %, and 0.52, respectively. Considering that multi-level methane concentration data are sparse if available at all, the NGM has the potential of an effective method for monitoring and modeling methane fluxes.

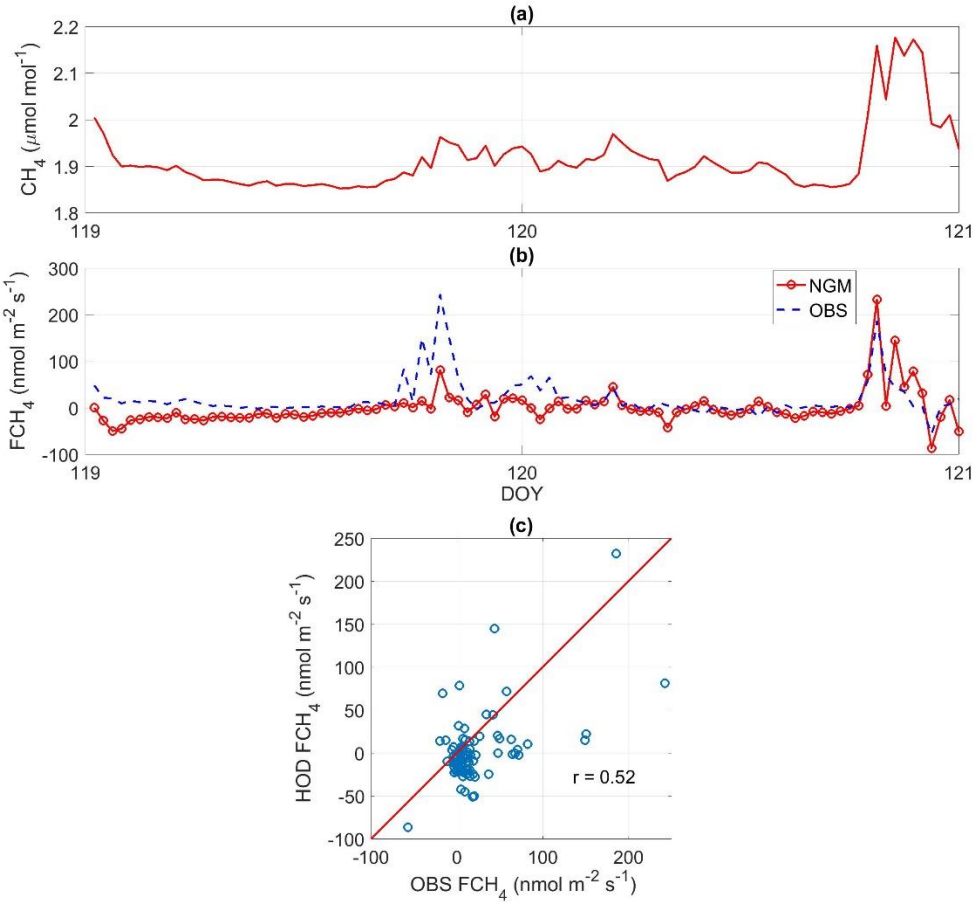

Figure 8. (a) CH_4, **(b)** and **(c)** NGM and OBS FCH_4 at US-Snd, Apr. 29 - May 1, 2007

5. Conclusion

This proof-of-concept study demonstrates the feasibility of surface gas fluxes derived from single-level near-surface gas concentration data using the newly formulated NGM model. One major advantage of the NGM is to avoid the use of gas concentration gradient data that are rarely available and subject to substantial measurement and/or modeling uncertainty. The parsimonious parameterization of eddy-diffusivity without explicit use of wind speed, surface roughness and vegetation specific data leads to reduced modeling uncertainty of the NGM gas fluxes. The case studies demonstrate the capability of the NGM in simulating diurnal and seasonal cycles of water vapor and CO_2 fluxes under diverse vegetation cover, geographic and climatic conditions. A preliminary test of the NGM for methane flux is encouraging. All validation tests support its potential for monitoring and modeling (greenhouse) gas fluxes at regional and global scale. We anticipate more independent tests of the NGM will follow to further evaluate its performance.

Appendix A: The derivation of Eqs. (2)-(4)

According to the extreme solution of the equations of MOST [*Wang and Bras*, 2010], D_c in Eq. (1) is written formally as

$$D_c = C_k \kappa z u_* \tag{A1}$$

where u_* is friction velocity, z the height above land surface, $\kappa (\approx 0.4)$ the von Karman constant, C_k a universal empirical constant associated with the atmospheric stability in the equations of MOST,

$$C_k = \begin{cases} \dfrac{2}{1+2\alpha}, H < 0 \text{ (stable)} \\ \dfrac{\sqrt{3}}{\alpha}, H > 0 \text{ (unsatble)} \end{cases}, \tag{A2}$$

where $\alpha \approx 1$. The extremum solute allows u_* to be expressed as a function of H,

$$u_* = \begin{cases} -\left(\dfrac{2\beta\kappa g H z}{\rho c_p T_r}\right)^{\frac{1}{3}}, H < 0 \\ \left(\dfrac{\gamma_2 \kappa g H z}{2\rho c_p T_r}\right)^{\frac{1}{3}}, H > 0 \end{cases} . \quad \text{(A3)}$$

where ρ ($\approx$ 1.2 kg m^{-3}) is the representative density of air, T_r ($\approx$ 300 K) the representative environment temperature, g (9.8 m s^{-2}) the gravitational acceleration, the universal empirical coefficients $\beta \sim 4.7$ and $\gamma_2 \sim 9$ [*Businger et al.*, 1971]. Combining Eqs. (A1) to (A3) leads to D_0 in Eq. (2),

$$D_0 = \begin{cases} \dfrac{2(2\beta)^{\frac{1}{3}}}{1+2\alpha}\left(\dfrac{g\kappa^4}{\rho c_p T_r}\right)^{\frac{1}{3}} \sim 1.25\times10^{-2}, H < 0 \\ \dfrac{\sqrt{3}}{\alpha}\left(\dfrac{\gamma_2}{2}\right)^{\frac{1}{3}}\left(\dfrac{g\kappa^4}{\rho c_p T_r}\right)^{\frac{1}{3}} \sim 2.54\times10^{-2}, H > 0 \end{cases} . \quad \text{(A4)}$$

Change of T_r from -10 °C to 30 °C only leads to 1% change of D_0. Hence, D_0 may be fixed as a constant in applications.

The derivation of Eq. (3) follows Oldham and Spanier [2006]. Assuming H being invariant with z within the surface layer [*Stull*, 1988], the change of variables $t' = \int_0^t |H(\tau)|^{\frac{1}{3}} d\tau$, $\xi = z^{\frac{1}{3}}$ and $A = \dfrac{D_0}{9}$ allows Eq. (1) to be re-written as,

$$\frac{\partial C}{\partial t'} = A\left(\frac{2}{\xi}\frac{\partial C}{\partial \xi} + \frac{\partial^2 C}{\partial \xi^2}\right). \quad \text{(A5)}$$

An analytical solution of Eq. (A5) in the spherical coordinates with the initial and boundary conditions of $C(\xi>0,t'=0)=C_0$, and $C(\xi\to\infty,t'>0)=C_0$ is given as (page 204 in [Oldham and Spanier [2006]),

$$\frac{\partial}{\partial\xi}C(\xi,t')=-\frac{1}{\sqrt{A}}\frac{\partial^{\frac{1}{2}}}{\partial t'^{\frac{1}{2}}}\left[C(\xi,t')-C_0\right]-\frac{C(\xi,t')-C_0}{\xi+R}, \tag{A6}$$

where R represents the radius of curvature of the surface. The half-order derivative ($\frac{d^{\frac{1}{2}}}{dt^{\frac{1}{2}}}$) of a function $f(t)$ is defined as,

$$\frac{d^{\frac{1}{2}}f(t)}{dt^{\frac{1}{2}}}\equiv\frac{1}{\sqrt{\pi}}\frac{d}{dt}\int_0^t\frac{f(\tau)d\tau}{\sqrt{t-\tau}}. \tag{A7}$$

For the case of the flat land surface, i.e. $\xi = 0$ and $R \to +\infty$, the last term of Eq. (A6) vanishes leading to,

$$\frac{\partial}{\partial\xi}C(\xi,t')=-\frac{1}{\sqrt{A}}\frac{\partial^{\frac{1}{2}}}{\partial t'^{\frac{1}{2}}}\left[C(\xi,t')-C_0\right], \tag{A8}$$

Substituting Eq. (A7) into Eq. (A8) and reversing the change of variables leads to Eq. (3)

$$F(z,t)\equiv-D_c(z,t)\frac{\partial C}{\partial z}=\frac{D_c(z,t)}{\sqrt{\pi}}\int_0^t\frac{\partial C(z,\tau)}{\partial\tau}\left[\int_\tau^t D_c(z,\zeta)d\zeta\right]^{-\frac{1}{2}}d\tau.$$

Eq. (3) reduces to Eq. (4) for the case of constant D_c

$$F_c(z,t)=\sqrt{\frac{D_c}{\pi}}\int_0^t\frac{\partial C(z,\tau)}{\partial\tau}\frac{d\tau}{\sqrt{t-\tau}}.$$

Figure A1 shows the variable and constant D_c using the hourly H data from the BR-Sa1 site. The variable D_c is calculated according to Eq. (2), and the constant D_c $(=6.2)$ is the time-averaged variable D_c. The variable D_c is physically more realistic for characterizing the diurnal variation of turbulent mixing.

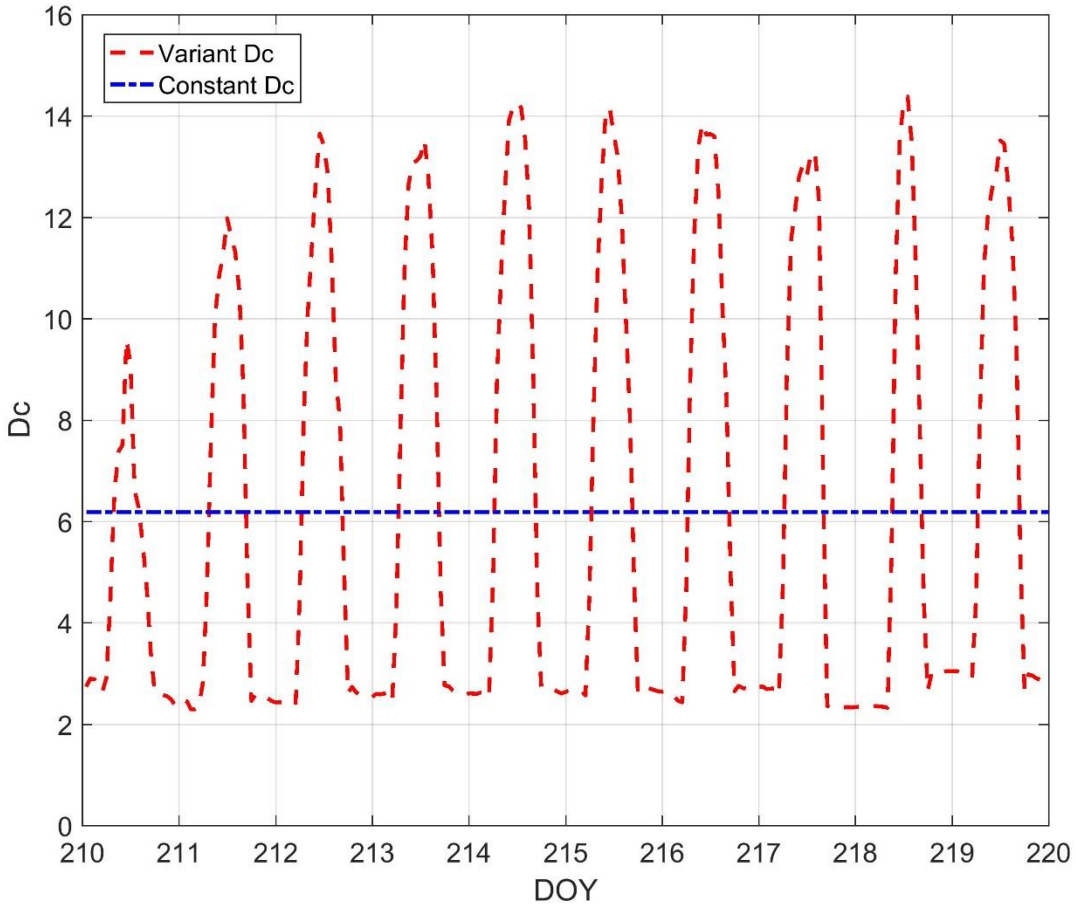

Figure A1. Variable and constant D_c at BR-Sa1, Jul. 29- Aug. 8, 2003

The sensitivity of F in Eq. (3) to the integration time is shown in Figure A2. The RMSE and NRMSE tend to decrease and r to increase quickly with the integration time t. The influence of initial value of C on F according to Eq. (3) diminishes after 48-hours, suggesting that it is sufficient to use two-day time-series data of C to compute F at a given time using Eq. (3).

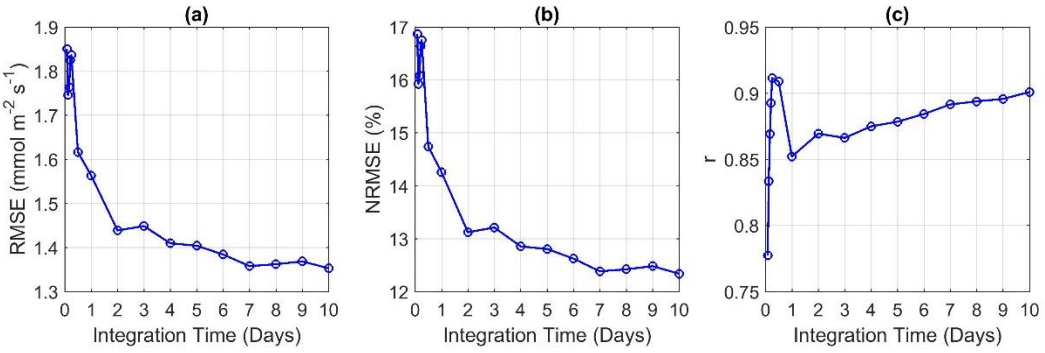

Figure A2. Sensitivity of F in Eq. (3) to integration time **(a)** RMSE, **(b)** NRMSE, and **(c)** r at BR-Sa1, Jul. 29- Aug. 8, 2003

Appendix B: Numerical algorithm for computing F in Eqs. (3) and (4)

Given the time-series data of C at $0 = t_0 < t_1 < t_2 < \cdots < t_N = t$, $F(z,t)$ can be calculated using the following numerical algorithm. To remove the singularity of the integrand, the double integral in Eq. (3) is re-written as,

$$\int_0^t \frac{\partial C(z,\tau)}{\partial \tau}\left[\int_\tau^t D_c(z,\zeta)d\zeta\right]^{-\frac{1}{2}} d\tau = -2\int_0^t \frac{\partial C(z,\tau)}{\partial \tau}\frac{1}{D_c(z,\tau)} d\left[\int_\tau^t D_c(z,\zeta)d\zeta\right]^{\frac{1}{2}}, \tag{B1}$$

where the differential is respect to τ. The integral on the right-hand-side of (B1) is the Rienmann-Stieltjes integral $\int_0^t f(\tau)dg(\tau)$ with

$$\begin{aligned} f(\tau) &= \frac{\partial C(z,\tau)}{\partial \tau}\frac{1}{D_c(z,\tau)}, \\ g(\tau) &= \left[\int_\tau^t D_c(z,\zeta)d\zeta\right]^{\frac{1}{2}}. \end{aligned} \tag{B2}$$

The Rienmann-Stieltjes integral may be numerically computed as

$$\int_0^t f(\tau)dg(\tau) = \sum_{i=1}^{N} f(t_i)[g(t_i) - g(t_{i-1})], \tag{B3}$$

where

$$f(t_i) = \frac{C(z,t_i) - C(z,t_{i-1})}{t_i - t_{i-1}} \frac{1}{D_c(z,t_i)},$$
$$g(t_i) = \left[\sum_{j=i+1}^{N} D_c(z,t_j)(t_j - t_{j-1}) \right]^{\frac{1}{2}}. \tag{B4}$$

$D_c(z,t_i)$ $(i = 1,\cdots,N)$ according to Eq. (2) is calculated using the MEP modeled $H(t_i)$. A sensitivity test of *F* to the time resolution of *C* data (Figure B1) indicates that coarser resolutions lead to higher RMSE and NRMSE and lower *r* as expected. Diurnal cycle of *F* is better captured by six-hourly or finer resolution data. 12-hourly or coarser resolution input data tend to miss the diurnal cycle. It is important to emphasize that the numerical algorithm (B4) does not require uniform integration time step, making the algorithm more flexible when the input data have missing points. Obviously, *F* will be more accurate with input data of finer time resolutions.

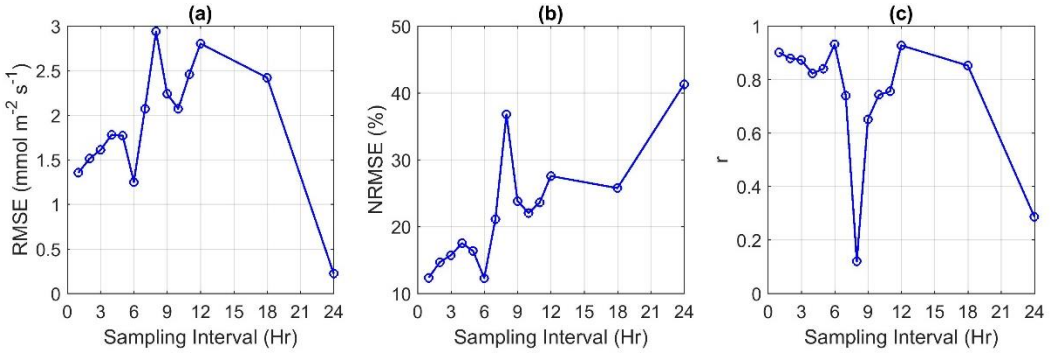

Figure B1. Sensitivity of *F* as in Eq. (3) to sampling intervals of *C* **(a)** RMSE, **(b)** NRMSE, and **(c)** *r* at BR-Sa1, Jul. 29- Aug. 8, 2003

The integral of Eq. (4) may be computed as

$$\sqrt{\frac{D_c}{\pi}}\int_0^t \frac{\partial C(z,\tau)}{\partial \tau}\frac{d\tau}{\sqrt{t-\tau}} \approx 2\sqrt{\frac{D_c}{\pi}}\sum_{i=0}^{N-1}\frac{C(\tau_{i+1})-C(\tau_i)}{\tau_{i+1}-\tau_i}\left(\sqrt{t-\tau_i}-\sqrt{t-\tau_{i+1}}\right) \tag{B5}$$

where $t = N\Delta t,\ \tau_i = i\Delta t,\ i = 0,1,\cdots,N\text{-}1$ with a uniform interval Δt. Eq. (B5) is a weighted integral of the time change rate of gas concentration and a time-dependent integration kernel

$$\sqrt{t-\tau_i}-\sqrt{t-\tau_{i+1}} = \sqrt{\Delta t}\left(\sqrt{N-i}-\sqrt{N-i-1}\right),\ i = 0,1,\cdots,N-1. \tag{B6}$$

The kernel in Eq. (B6) for $N = 48, \Delta t = 1$ hr (Figure B2) demonstrates the fast-decaying influence of *C* at earlier times on the NGM *C* at current time. As a result, unrealistic C only has large impacts on the NGM flux at the current time step and little impacts on the flux as time proceeds so that the NGM flux agrees with the OBS flux again several time steps after the spikes as shown in Figures 2 and 4.

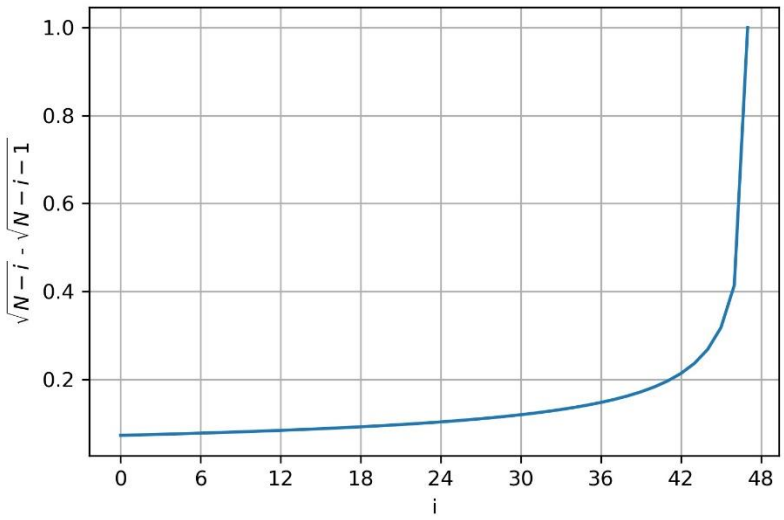

Figure B2. Decays from the current integrand to the initial integrand for a 48-step integration.

Appendix C: The MEP model of heat fluxes over land surfaces

The MEP model is built on the contemporary non-equilibrium thermodynamics, the Bayesian probability theory, information theory, and well-established atmospheric boundary layer turbulence theory [*Wang and Bras*, 2009; 2011]. The MEP model simulates the partition of radiation fluxes into surface turbulent and conductive heat fluxes, automatically balancing the surface energy budget using fewer model parameters than existing models such as the bulk transfer models. The MEP model does not use temperature/moisture gradient, wind speed, surface roughness and stomatal/aerodynamic conductance parameters. The MEP model has been extensively tested for modeling land surface heat fluxes [*Wang and Bras*, 2009; 2011; *Nearing et al.*, 2012; *Wang et al.*, 2014; *Yang and Wang*, 2014b; *Shanafield et al.*, 2015; *Huang et al.*, 2016; *Wang et al.*, 2017; *Hajji et al.*, 2018; *El Sharif et al.*, 2019; *Li et al.*, 2019; *Xu et al.*, 2019].

The MEP fluxes are solved for by minimizing the irreversibility or dissipation function defined as

$$D(E,H,G) = \frac{2G^2}{I_s} + \frac{2H^2}{I_a} + \frac{2E^2}{I_e} \tag{C1}$$

under the constraint of surface energy balance $E + H + G = R_n$, where I_s, I_a, and I_e ($W\ m^{-2}K^{-1}s^{\frac{1}{2}}$) are the thermal inertia parameters associated with ground (G), sensible (H) and latent (E) heat flux. I_a is parameterized using the extreme solution of the equations of MOST [*Wang and Bras*, 2011],

$$I_a = \rho c_p \sqrt{C_1 \kappa z} \left(\frac{C_2 \kappa z g}{\rho C_p T_s}\right)^{\frac{1}{6}} |H|^{\frac{1}{6}} = I_0 |H|^{\frac{1}{6}} \tag{C2}$$

where C_1 and C_2 are coefficients related to the universal constants in the MOSE [*Businger et al.*, 1971],

$$C_1 = \begin{cases} \sqrt{3}, & H > 0 \\ \dfrac{2}{3}, & H < 0 \end{cases}, \quad C_2 = \begin{cases} \dfrac{\gamma_2}{2}, & H > 0 \\ 2\beta, & H < 0 \end{cases} \tag{C3}$$

with the empirical constants $\gamma_2 \sim 9, \beta \sim 5$.

I_e is parameterized as [*Wang and Bras*, 2011].

$$I_e = \sigma I_a, \quad \sigma \equiv \frac{\lambda^2}{R_v c_p} \frac{q_s}{T_s^2} \tag{C4}$$

where T_s is surface temperature and q_s surface specific humidity with the latent heat of vaporization λ (2.5×10^6 J kg^{-1}), gas constant of water vapor R_v (461 J kg^{-1} K^{-1}) and specific heat of air at constant pressure c_p (10^3 J kg^{-1}K^{-1}). Minimizing *D* in Eq. (C1) leads to

$$\begin{aligned} &G = \frac{B(\sigma)}{\sigma} \frac{I_s}{I_0} H |H|^{-\frac{1}{6}}, \; E = B(\sigma) H, \; E + H + G = R_n \\ &B(\sigma) \equiv 6\left(\sqrt{1 - \frac{11}{36}\sigma} - 1 \right) \end{aligned} \tag{C5}$$

where $B(\sigma)$ is the MEP predicted reciprocal Bowen ratio. Over the land surfaces covered with dense canopy $I_s \approx 0, \; G \approx 0$, Eq. (C5) reduces to Eq. (5).

Acknowledgements

This study is sponsored by NSF CZO program Grant EAR-1331846. Partial support is provided by NASA NEWS program grant NNX15AT41G. AmeriFlux network (http://ameriflux.ornl.gov/) is funded by the U.S. Department of Energy's Office of Science.

References

Anthoni, P. M., B. E. Law, and M. H. Unsworth (1999), Carbon and water vapor exchange of an open-canopied ponderosa pine ecosystem, *Agric. For. Meteorol.*, *95*(3), 151-168, doi:Doi 10.1016/S0168-1923(99)00029-5.

Arya, S. P. (2001), *Introduction to Micrometeorology*, Academic Press.

Aubinet, M. (2008), Eddy covariance CO2 flux measurements in nocturnal conditions: an analysis of the problem, *Ecol Appl*, *18*(6), 1368-1378, doi:10.1890/06-1336.1.

Aubinet, M., T. Vesala, and D. Papale (2012), *Eddy Covariance: A Practical Guide to Measurement and Data Analysis*, Springer Netherlands.

Baldocchi, D. D. (2003), Assessing the eddy covariance technique for evaluating carbon dioxide exchange rates of ecosystems: past, present and future, *Global Change Biol.*, *9*(4), 479-492, doi:DOI 10.1046/j.1365-2486.2003.00629.x.

Barr, A. G., K. Morgenstern, T. A. Black, J. H. McCaughey, and Z. Nesic (2006), Surface energy balance closure by the eddy-covariance method above three boreal forest stands and implications for the measurement of the CO2 flux, *Agric. For. Meteorol.*, *140*(1-4), 322-337, doi:10.1016/j.agrformet.2006.08.007.

Basilio, R., M. Bennett, A. Eldering, P. Lawson, and R. Rosenberg (2019), *Orbiting Carbon Observatory-3 (OCO-3), remote sensing from the International Space Station (ISS)*, SPIE.

Basu, S., and A. Lacser (2017), A cautionary note on the use of Monin–Obukhov similarity theory in very high-resolution large-eddy simulations, *Boundary-Layer Meteorology*, *163*(2), 351-355.

Beck, J. V., S. C. Jr, B. Blackwell, C. R. S. Clair, and C. R. S. Clair (1985), *Inverse Heat Conduction: Ill-Posed Problems*, Wiley.

Beltrami, H., J. Wang, and R. L. Bras (2000), Energy balance at the Earth's surface: Heat flux history in eastern Canada, *Geophys. Res. Lett.*, *27*(20), 3385-3388, doi:10.1029/2000GL008483.

Bennett, W. B., J. Wang, and R. L. Bras (2008), Estimation of global ground heat flux, *J. Hydrometeorol.*, *9*(4), 744-759, doi:10.1175/2008JHM940.1.

Brienen, R. J., et al. (2015), Long-term decline of the Amazon carbon sink, *Nature*, *519*(7543), 344-348, doi:10.1038/nature14283.

Burba, G. (2013), *Eddy covariance method for scientific, industrial, agricultural and regulatory applications: A field book on measuring ecosystem gas exchange and areal emission rates*, LI-Cor Biosciences.

Businger, J. A., J. C. Wyngaard, Y. Izumi, and E. F. Bradley (1971), Flux-Profile Relationships in the Atmospheric Surface Layer, *J. Atmos. Sci.*, *28*(2), 181-189, doi:10.1175/1520-0469(1971)028<0181:fprita>2.0.co;2.

Cellier, P. (1986), On the validity of flux-gradient relationships above very rough surfaces, *Boundary-Layer Meteorology*, *36*(4), 417-419, doi:10.1007/bf00118340.

Collatz, G. J., J. T. Ball, C. Grivet, and J. A. Berry (1991), Physiological and environmental regulation of stomatal conductance, photosynthesis and transpiration: a model that includes a laminar boundary layer, *Agric. For. Meteorol.*, *54*(2–4), 107-136, doi:10.1016/0168-1923(91)90002-8.

da Rocha, H. R., M. L. Goulden, S. D. Miller, M. C. Menton, L. D. V. O. Pinto, H. C. de Freitas, and A. M. e Silva Figueira (2004), Seasonality of Water and Heat Fluxes over a Tropical Forest in Eastern Amazonia, *Ecol. Appl.*, *14*(sp4), 22-32, doi:10.1890/02-6001.

Dold, C., H. Büyükcangaz, W. Rondinelli, J. H. Prueger, T. J. Sauer, and J. L. Hatfield (2017), Long-term carbon uptake of agro-ecosystems in the Midwest, *Agric. For. Meteorol.*, *232*, 128-140, doi:https://doi.org/10.1016/j.agrformet.2016.07.012.

El Sharif, H., W. Zhou, V. Ivanov, A. Sheshukov, V. Mazepa, and J. Wang (2019), Surface Energy Budgets of Arctic Tundra During Growing Season, *J. Geophys. Res. D: Atmos.*, *124*(13), 6999-7017, doi:https://doi.org/10.1029/2019JD030650.

Falge, E., et al. (2001), Gap filling strategies for defensible annual sums of net ecosystem exchange, *Agric. For. Meteorol.*, *107*(1), 43-69, doi:Doi 10.1016/S0168-1923(00)00225-2.

Franks, P. J., D. L. Royer, D. J. Beerling, P. K. Van de Water, D. J. Cantrill, M. M. Barbour, and J. A. Berry (2014), New constraints on atmospheric CO2 concentration for the Phanerozoic, *Geophys. Res. Lett.*, *41*(13), 4685-4694, doi:10.1002/2014gl060457.

Gao, Z., E. S. Russell, J. E. Missik, M. Huang, X. Chen, C. E. Strickland, R. Clayton, E. Arntzen, Y. Ma, and H. Liu (2017), A novel approach to evaluate soil heat flux calculation: An analytical review of nine methods, *J. Geophys. Res. D: Atmos.*, *122*(13), 6934-6949.

Gatti, L. V., et al. (2014), Drought sensitivity of Amazonian carbon balance revealed by atmospheric measurements, *Nature*, *506*(7486), 76-80, doi:10.1038/nature12957.

Gopalakrishnan, S. G., F. Marks, J. A. Zhang, X. Zhang, J.-W. Bao, and V. Tallapragada (2013), A Study of the Impacts of Vertical Diffusion on the Structure and Intensity of the Tropical Cyclones Using the High-Resolution HWRF System, *J. Atmos. Sci.*, *70*(2), 524-541, doi:10.1175/jas-d-11-0340.1.

Goulden, M. L., J. W. Munger, S. M. Fan, B. C. Daube, and S. C. Wofsy (1996), Measurements of carbon sequestration by long-term eddy covariance: Methods and a critical evaluation of accuracy, *Global Change Biol.*, *2*(3), 169-182, doi:DOI 10.1111/j.1365-2486.1996.tb00070.x.

Gu, L. H., et al. (2005), Objective threshold determination for nighttime eddy flux filtering, *Agric. For. Meteorol.*, *128*(3-4), 179-197, doi:10.1016/j.agrformet.2004.11.006.

Hajji, I., D. F. Nadeau, B. Music, F. Anctil, and J. Wang (2018), Application of the Maximum Entropy Production Model of Evapotranspiration over Partially Vegetated Water-Limited Land Surfaces, *J. Hydrometeorol.*, *19*(6), 989-1005, doi:10.1175/jhm-d-17-0133.1.

Hatala, J. A., M. Detto, O. Sonnentag, S. J. Deverel, J. Verfaillie, and D. D. Baldocchi (2012), Greenhouse gas (CO2, CH4, H2O) fluxes from drained and flooded agricultural peatlands in the Sacramento-San Joaquin Delta, *Agriculture Ecosystems & Environment*, *150*(Supplement C), 1-18, doi:10.1016/j.agee.2012.01.009.

Hilfer, R. (2000), *Applications of Fractional Calculus in Physics*, doi:10.1142/3779.

Hollinger, D. Y., and A. D. Richardson (2005), Uncertainty in eddy covariance measurements and its application to physiological models, *Tree Physiol.*, *25*(7), 873-885, doi:10.1093/treephys/25.7.873.

Hsieh, C.-I., C.-W. Huang, and G. Kiely (2009), Long-term estimation of soil heat flux by single layer soil temperature, *International Journal of Biometeorology*, *53*(1), 113-123, doi:10.1007/s00484-008-0198-8.

Huang, S.-Y., Y. Deng, and J. Wang (2016), Revisiting the global surface energy budgets with maximum-entropy-production model of surface heat fluxes, *Clim. Dyn.*, *49*(5-6), 1531-1545, doi:10.1007/s00382-016-3395-x.

Kroon, P. S., A. Hensen, H. J. J. Jonker, H. G. Ouwersloot, A. T. Vermeulen, and F. C. Bosveld (2010), Uncertainties in eddy covariance flux measurements assessed from CH4 and N2O observations, *Agric. For. Meteorol.*, *150*(6), 806-816, doi:10.1016/j.agrformet.2009.08.008.

Lee, T. J., and R. A. Pielke (1992), Estimating the Soil Surface Specific Humidity, *Journal of Applied Meteorology*, *31*(5), 480-484, doi:10.1175/1520-0450(1992)031<0480:etsssh>2.0.co;2.

Li, N., P. Zhao, J. Wang, and Y. Deng (2019), Estimation of Surface Heat Fluxes Over the Central Tibetan Plateau using the Maximum Entropy Production Model, *J. Geophys. Res. D: Atmos.*, *124*(13), 6827-6840, doi:https://doi.org/10.1029/2018JD029959.

Miller, K. S., and B. Ross (1993), An introduction to the fractional calculus and fractional differential equations, *Wiley, New York*.

Miller, R. M., S. P. Miller, J. D. Jastrow, and C. B. Rivetta (2002), Mycorrhizal mediated feedbacks influence net carbon gain and nutrient uptake in Andropogon gerardii, *New Phytologist*, *155*(1), 149-162, doi:doi:10.1046/j.1469-8137.2002.00429.x.

Monteith, J., and M. Unsworth (2013), *Principles of Environmental Physics: Plants, Animals, and the Atmosphere*, Elsevier Science.

Morin, T. H., G. Bohrer, K. C. Stefanik, A. C. Rey-Sanchez, A. M. Matheny, and W. J. Mitsch (2017), Combining eddy-covariance and chamber measurements to determine the methane budget from a small, heterogeneous urban floodplain wetland park, *Agric. For. Meteorol.*, *237*, 160-170, doi:10.1016/j.agrformet.2017.01.022.

Nearing, G. S., M. S. Moran, R. L. Scott, and G. Ponce-Campos (2012), Coupling diffusion and maximum entropy models to estimate thermal inertia, *Remote Sens. Environ.*, *119*, 222-231, doi:10.1016/j.rse.2011.12.012.

Nicolini, G., et al. (2018), Impact of CO2 storage flux sampling uncertainty on net ecosystem exchange measured by eddy covariance, *Agric. For. Meteorol.*, *248*, 228-239, doi:https://doi.org/10.1016/j.agrformet.2017.09.025.

Nieuwstadt, F. T. M. (1980), An Analytic Solution of the Time-Dependent, One-Dimensional Diffusion Equation in the Atmospheric Boundary-Layer, *Atmos. Environ.*, *14*(12), 1361-1364, doi:Doi 10.1016/0004-6981(80)90154-7.

Nieves, V., J. Wang, and J. Willis (2014), A conceptual model of ocean freshwater flux derived from sea surface salinity, *Geophys. Res. Lett.*, *41*(18), 6452-6458, doi:10.1002/2014GL061365.

Nishimoto, K. (1991), *An Essence of Nishimoto's Fractional Calculus: (calculus in the 21st Century) : Integrations and Differentiations of Arbitrary Order*, Descartes Press.

Oldham, K. B., and J. Spanier (2006), *The Fractional Calculus: Theory and Applications of Differentiation and Integration to Arbitrary Order*, Dover Publications.

Philip, J. R. (1957), EVAPORATION, AND MOISTURE AND HEAT FIELDS IN THE SOIL, *Journal of Meteorology*, *14*(4), 354-366, doi:10.1175/1520-0469(1957)014<0354:eamahf>2.0.co;2.

Phillips, O. L., et al. (2009), Drought sensitivity of the Amazon rainforest, *Science*, *323*(5919), 1344-1347, doi:10.1126/science.1164033.

Post, H., H. J. H. Franssen, A. Graf, M. Schmidt, and H. Vereecken (2015), Uncertainty analysis of eddy covariance CO2 flux measurements for different EC tower distances using an extended two-tower approach, *Biogeosciences*, *12*(4), 1205-1221, doi:10.5194/bg-12-1205-2015.

Purdy, A. J., J. B. Fisher, M. L. Goulden, and J. S. Famiglietti (2016), Ground heat flux: An analytical review of 6 models evaluated at 88 sites and globally, *Journal of Geophysical Research: Biogeosciences*, *121*(12), 3045-3059, doi:https://doi.org/10.1002/2016JG003591.

Ramírez- Beltrán, N. D., C. M. Salazar, J. M. Castro Sánchez, and J. E. González (2019), A satellite algorithm for estimating relative humidity, based on GOES and MODIS satellite data,

International Journal of Remote Sensing, *40*(24), 9237-9259, doi:10.1080/01431161.2019.1629715.

Richardson, A. D., et al. (2006), Comparing simple respiration models for eddy flux and dynamic chamber data, *Agric. For. Meteorol.*, *141*(2-4), 219-234, doi:10.1016/j.agrformet.2006.10.010.

Saleska, S. R., et al. (2003), Carbon in Amazon forests: unexpected seasonal fluxes and disturbance-induced losses, *Science*, *302*(5650), 1554-1557, doi:10.1126/science.1091165.

Samko, S. G., A. A. Kilbas, and O. I. Marichev (1993), *Fractional integrals and derivatives*, Gordon and Breach Science Publishers, Yverdon Yverdon-les-Bains, Switzerland.

Schimel, D. S. (1995), Terrestrial Ecosystems and the Carbon-Cycle, *Global Change Biol.*, *1*(1), 77-91, doi:DOI 10.1111/j.1365-2486.1995.tb00008.x.

Sellers, P. J., et al. (1997), Modeling the exchanges of energy, water, and carbon between continents and the atmosphere, *Science*, *275*(5299), 502-509, doi:DOI 10.1126/science.275.5299.502.

Sellers, P. J., D. A. Randall, G. J. Collatz, J. A. Berry, C. B. Field, D. A. Dazlich, C. Zhang, G. D. Collelo, and L. Bounoua (1996), A Revised Land Surface Parameterization (SiB2) for Atmospheric GCMS. Part I: Model Formulation, *Journal of Climate*, *9*(4), 676-705, doi:10.1175/1520-0442(1996)009<0676:arlspf>2.0.co;2.

Shanafield, M., P. G. Cook, H. A. Gutierrez-Jurado, R. Faux, J. Cleverly, and D. Eamus (2015), Field comparison of methods for estimating groundwater discharge by evaporation and evapotranspiration in an arid-zone playa, *J. Hydrol.*, *527*, 1073-1083, doi:10.1016/j.jhydrol.2015.06.003.

Stoffelen, A., et al. (2020), Wind Profile Satellite Observation Requirements and Capabilities, *Bulletin of the American Meteorological Society*, *101*(11), E2005-E2021, doi:10.1175/bams-d-18-0202.1.

Stull, R. B. (1988), *An Introduction to Boundary Layer Meteorology*, Springer Netherlands.

Thomas, C., J. G. Martin, M. Goeckede, M. B. Siqueira, T. Foken, B. E. Law, H. W. Loescher, and G. Katul (2008), Estimating daytime subcanopy respiration from conditional sampling methods applied to multi-scalar high frequency turbulence time series, *Agric. For. Meteorol.*, *148*(8-9), 1210-1229, doi:10.1016/j.agrformet.2008.03.002.

Thomas, C. K., J. G. Martin, B. E. Law, and K. Davis (2013), Toward biologically meaningful net carbon exchange estimates for tall, dense canopies: Multi-level eddy covariance observations and canopy coupling regimes in a mature Douglas-fir forest in Oregon, *Agric. For. Meteorol.*, *173*, 14-27, doi:10.1016/j.agrformet.2013.01.001.

Tian, H. Q., J. M. Melillo, D. W. Kicklighter, A. D. McGuire, J. V. K. Helfrich, B. Moore, and C. J. Vorosmarty (1998), Effect of interannual climate variability on carbon storage in Amazonian ecosystems, *Nature*, *396*(6712), 664-667, doi:Doi 10.1038/25328.

Ullmann, T., and G. Stauch (2020), Surface Roughness Estimation in the Orog Nuur Basin (Southern Mongolia) Using Sentinel-1 SAR Time Series and Ground-Based Photogrammetry, *Remote Sensing*, *12*(19), 3200.

Verma, M., et al. (2016), Global Surface Net-Radiation at 5 km from MODIS Terra, *Remote Sensing*, *8*(9), 739.

Vickers, D., M. Gockede, and B. E. Law (2010), Uncertainty estimates for 1-h averaged turbulence fluxes of carbon dioxide, latent heat and sensible heat, *Tellus Series B-Chemical and Physical Meteorology*, *62*(2), 87-99, doi:10.1111/j.1600-0889.2009.00449.x.

Wang, H. L., D. Tetzlaff, and C. Soulsby (2017), Testing the maximum entropy production approach for estimating evapotranspiration from closed canopy shrubland in a low-energy humid environment, *Hydrol. Processes*, *31*(25), 4613-4621, doi:10.1002/hyp.11363.

Wang, J., and R. L. Bras (1999), Ground heat flux estimated from surface soil temperature, *J. Hydrol.*, *216*(3-4), 214-226, doi:Doi 10.1016/S0022-1694(99)00008-6.

Wang, J., and R. L. Bras (2009), A model of surface heat fluxes based on the theory of maximum entropy production, *Water Resour. Res.*, *45*(11), W11422, doi:10.1029/2009wr007900.

Wang, J., and R. L. Bras (2010), An Extremum Solution of the Monin–Obukhov Similarity Equations, *J. Atmos. Sci.*, *67*(2), 485-499, doi:10.1175/2009jas3117.1.

Wang, J., and R. L. Bras (2011), A model of evapotranspiration based on the theory of maximum entropy production, *Water Resour. Res.*, *47*(3), n/a-n/a, doi:10.1029/2010wr009392.

Wang, J., R. L. Bras, V. Nieves, and Y. Deng (2014), A model of energy budgets over water, snow, and ice surfaces, *Journal of Geophysical Research-Atmospheres*, *119*(10), 6034-6051, doi:10.1002/2013jd021150.

Wang, K. C., and R. E. Dickinson (2012), A Review of Global Terrestrial Evapotranspiration: Observation, Modeling, Climatology, and Climatic Variability, *Rev. Geophys.*, *50*(2), n/a-n/a, doi:10.1029/2011rg000373.

Wang, Z.-H. (2012), Reconstruction of soil thermal field from a single depth measurement, *J. Hydrol.*, *464-465*, 541-549, doi:https://doi.org/10.1016/j.jhydrol.2012.07.047.

Wilson, K. B., P. J. Hanson, P. J. Mulholland, D. D. Baldocchi, and S. D. Wullschleger (2001), A comparison of methods for determining forest evapotranspiration and its components: sap-flow, soil water budget, eddy covariance and catchment water balance, *Agric. For. Meteorol.*, *106*(2), 153-168, doi:Doi 10.1016/S0168-1923(00)00199-4.

Xu, D., E. Agee, J. Wang, and V. Y. Ivanov (2019), Estimation of Evapotranspiration of Amazon Rainforest Using the Maximum Entropy Production Method, *Geophys. Res. Lett.*, *0*(0), doi:doi:10.1029/2018GL080907.

Yang, J., and Z.-H. Wang (2014a), Land surface energy partitioning revisited: A novel approach based on single depth soil measurement, *Geophys. Res. Lett.*, *41*(23), 8348-8358, doi:https://doi.org/10.1002/2014GL062041.

Yang, J., Z.-H. Wang, Q. Li, N. Vercauteren, E. Bou-Zeid, and M. B. Parlange (2017), A novel approach for unraveling the energy balance of water surfaces with a single depth temperature measurement, *Limnology and Oceanography*, *62*(1), 89-103, doi:https://doi.org/10.1002/lno.10378.

Yang, J. C., and Z. H. Wang (2014b), Land surface energy partitioning revisited: A novel approach based on single depth soil measurement, *Geophys. Res. Lett.*, *41*(23), 8348-8358, doi:10.1002/2014gl062041.

Yang, P., E. Prikaziuk, W. Verhoef, and C. van der Tol (2020), SCOPE 2.0: A model to simulate vegetated land surface fluxes and satellite signals, *Geosci. Model Dev. Discuss.*, *2020*, 1-26, doi:10.5194/gmd-2020-251.

Zhu, W., B. Wu, N. Yan, X. Feng, and Q. Xing (2014), A method to estimate diurnal surface soil heat flux from MODIS data for a sparse vegetation and bare soil, *J. Hydrol.*, *511*, 139-150, doi:https://doi.org/10.1016/j.jhydrol.2014.01.019.